RSC Advances

Check for updates

Exploring the peroxidase-like activity of 4Fe–Ni–B nanoparticles for analytical sensing†

Si-Hua Deng, [ID] Ying-Zhao Ma, [ID] Yi-Fan Han, Qi Zhou [ID]* and Wen-Sheng Fu*

Natural enzymes, despite their superior catalytic proficiency, are frequently constrained by their environmental sensitivity and the intricacies associated with their extraction and preservation. Consequently, there has been a significant impetus in the scientific community to develop robust, economical, and accessible enzyme mimics. In this context, transition metal borides have risen to prominence as auspicious contenders, capitalizing on their distinctive electronic and catalytic attributes to replicate the functionalities of natural enzymes. In our present investigation, we report the synthesis of amorphous metal boride nanoparticles utilizing a straightforward chemical reduction approach conducted under refrigerated conditions. Notably, it is within this study that these nanoparticles are first showcased to exhibit inherent peroxidase-like activity, with the 4Fe–Ni–B composition demonstrating superior catalytic activity compared to other tested samples. Density functional theory (DFT) calculations have elucidated that the incorporation of nickel significantly bolsters the reactivity of 4Fe–Ni–B towards hydrogen peroxide (H_2O_2). This enhancement stems from a synergistic interaction between Ni^{2+} and Fe^{3+} ions, which expedites the reduction of Fe^{3+} to Fe^{2+}, consequently augmenting the overall catalytic efficacy. To further broaden the applicative scope of these nanozymes, we have developed a colorimetric sensor for the rapid detection of H_2O_2 and glutathione (GSH), thereby underscoring the adaptability of transition metal borides in analytical chemistry.

1 Introduction

Enzymes, the quintessential biocatalysts, are renowned for their exceptional catalytic efficiency and precise substrate selectivity.[1] Despite these virtues, the broad application of enzymes is often thwarted by their inherent instability, the complexity of their purification processes, the stringent conditions required for their preservation, and the high costs associated with their production and maintenance. Consequently, the scientific community has channeled significant effort to the study of enzyme mimics—artificial constructs that replicate the structural and functional attributes of their natural counterparts. This rapidly evolving domain includes a diverse array of mimics, such as superoxide dismutase, catalase, peroxidase, oxidase, and nuclease, each offering potential across a spectrum of applications.[2]

Particularly noteworthy are the merits of nanomaterial-based mimics of natural enzymes, which have garnered significant interest due to their affordability, straightforward synthesis, and adjustable catalytic activity.[3] These nanomaterial-based mimics have been the subject of extensive research for

a myriad of applications, spanning from *in vitro* sensing and biomedical therapeutics to cancer treatment and environmental quality assessment.[4,5] In a seminal study, Yan *et al.* first reported that Fe_3O_4 ferromagnetic nanoparticles exhibit intrinsic peroxidase-like activity.[6] This discovery has since been followed by the identification of a plethora of nanomaterials, including metal oxides,[7–9] bimetallic oxides,[10–12] metallic and alloyed structures,[13–17] metal–organic frameworks,[18–20] metal sulfides,[21,22] and carbon-based nanomaterials,[23–25] all of which have demonstrated inherent enzyme-mimicking capabilities. These materials are extensively utilized in the detection of a variety of analytes, such as DNA, H_2O_2, glucose, heavy metal ions, and other substances.[26,27] Recently, the strategic formation of "metal–nonmetal" bridges within nanoenzymatic catalysts, achieved by incorporating sulfur into their structure, has been proposed to amplify their catalytic prowess. These bridges are believed to induce a cooperative metal-to-metal interaction and bolster electron transfer at the catalytically active sites.[28–32] For instance, Zhang *et al.* synthesized Fe–N–S–C by sulfur-functionalizing Fe–N–C, thereby modulating the active oxygen species in single-atom nanoenzymes.[33] Their findings indicated that this functionalization led to a significant modification of the electronic structure of Fe–N–S–C. Specifically, there was an observed increase in electron density at the Fermi energy level, which correlated with an enhanced electron transfer efficiency from the active site to the critical intermediate *OOH.

Chongqing Key Laboratory of Green Catalysis Materials and Technology, College of Chemistry, Chongqing Normal University, Chongqing 401331, China. E-mail: zhouqi@cqnu.edu.cn; fuwensheng@cqnu.edu.cn

Additionally, it has been proposed that the introduction of oxygen vacancies could be instrumental in constructing nano-enzymes with engineered defects. Such defect-enriched structures serve as pivotal charge separation centers, thereby amplifying electron transfer capabilities. In a related development, Wang *et al.* synthesized the multifunctional nano-enzymes Ox-POM@Cu, which incorporated OVs.[34] The presence of OVs was found to expedite electron transfer processes, subsequently augmenting the GPx and CAT-like activities of Ox-POM@Cu.

Beyond these advancements, boron, a non-metallic element, has been recognized for its pivotal role in fine-tuning the electronic structure of catalysts and in fostering the emergence of active sites. As a result, metal boride nanomaterials, with their remarkable electrocatalytic properties and broad applicability in catalytic processes, have garnered significant attention within the scientific community. Despite the burgeoning interest in nano-enzymatic systems, the literature on modulating their enzymatic activity remains sparse. Notably, amorphous nanoparticles of FeB are characterized by an abundance of surface defects and coordination unsaturation sites, which endow their electronic structure with a high degree of tunability. This flexibility arises from the capacity to form amorphous structures from a diverse array of constituents, a feature that crystalline forms cannot replicate. Furthermore, elemental iron, due to its variable valence states, manifests peroxidase-like activity, while elemental nickel, similarly characterized by variable valence, serves as a cofactor in numerous metal nanoenzymes.[35] Given these desirable yet abundant properties, the design and construction of amorphous structured bimetallic borides offer compelling opportunities to advance the field of nanoenzymes. To our knowledge, however, the peroxidase-like activity of metal boride nanoparticles remains unexplored within the realm of natural enzyme mimics.

In our current study, we report for the first time the intrinsic peroxidase mimetic activity of metal boride nanoparticles. Through a facile chemical reduction approach, we successfully synthesized these nanomaterials, which notably catalyzed the oxidation of 3,3′,5,5′-tetramethylbenzidine (TMB) in the presence of H_2O_2, effecting a distinct color change from colorless to blue. This reaction emulates the catalytic behavior of natural peroxidases. Delving into the underlying mechanism, we discovered the pivotal role of Fe^{2+} and Fe^{3+} ions as active sites within the xFe-5-xNi–B framework. Density functional theory (DFT) calculations elucidated that the introduction of nickel into the 4Fe–Ni–B structure markedly enhanced its responsiveness to hydrogen peroxide and key reaction intermediates. Our findings highlight the synergistic interaction between Ni^{2+} and Fe^{3+} ions as a critical factor in augmenting the nanozyme's catalytic activity, facilitating the conversion of Fe^{3+} to Fe^{2+} and thereby enhancing the overall catalytic efficiency. To further broaden the applicability of these nanozymes, we have developed a colorimetric sensor designed for the swift and accurate detection of H_2O_2 and GSH, as shown in Scheme 1. This innovation underscores the adaptability of metal boride nanoparticles in a variety of analytical applications. Our research not
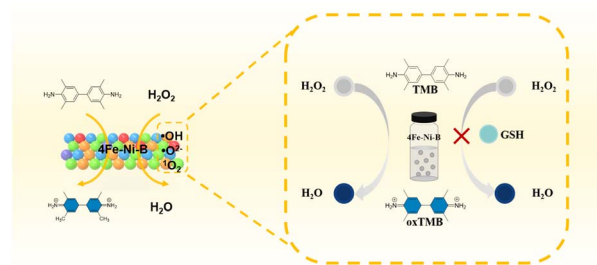
Scheme 1 A 4Fe−Ni−B based design for peroxide-like as enzyme and colorimetric detection of glutathione application.

only advances the frontier of binary metal borides as substitutes for natural enzymes but also deepens the comprehension of nanozyme design paradigms. This advancement opens up new horizons for the development of next-generation artificial enzymes capable of exhibiting customized catalytic profiles tailored to specific applications.

2 Method

2.1 Synthesis of Fe–B/Ni–B

Fe–B/Ni–B was synthesized according to the ref. 28. Briefly, 20 mmol $FeSO_4 \cdot 7H_2O$ (or $NiCl_2 \cdot 6H_2O$) were solubilized in 40 mL of DI water under intense mixing in an ice-water bath. After continuously passing nitrogen gas for 20 minutes, 60 mL of a mixed solution of $NaBH_4$ (1 M) and NaOH (0.1 M) was dropped at a rate of 2 mL min^{-1} using a constant pressure funnel. The solution was then agitated in an ice bath for another 30 minutes, and the solid sample was washed with DI and ethanol filtration. The purified sample was dried under vacuum at 60 °C overnight, and a black powder was obtained by grinding.

2.2 Synthesis of xFe-5-xNi–B

The preparation of amorphous xFe-5-xNi–B nanoparticles was achieved through a chemical reduction approach. We initiated the process by dissolving varying proportions of $FeSO_4 \cdot 7H_2O$ in amounts of 18 mmol, 16 mmol, 12 mmol, and 8 mmol, along with $NiCl_2 \cdot 6H_2O$ in amounts of 2 mmol, 4 mmol, 8 mmol, and 12 mmol, into 40 mL of deionized water. This mixture was subjected to vigorous stirring within an ice-water bath to ensure homogeneity. Under a continuous flow of nitrogen gas for 20 minutes to maintain an inert atmosphere, 60 mL of a mixed solution consisting of $NaBH_4$ (1 M) and NaOH (0.1 M) was added dropwise at a rate of 2 mL per minute using a constant pressure funnel. Following the addition, the mixture was stirred in an ice bath for an additional 30 minutes to facilitate the reduction reaction. The resulting solid was then isolated and washed through filtration with water and ethanol to remove any unreacted precursors. The purified solid sample was subsequently dried under vacuum at 60 °C for an entire night. The final product was a black powder obtained by grinding the dried solid. These synthesized samples, designated as 4.5Fe–0.5Ni–B, 4Fe–Ni–B, 3Fe–2Ni–B, and 2Fe–3Ni–B, correspond to the initial

concentrations of iron and nickel salts used in the reaction mixture.

2.3 Detection of GSH

Normally, 0.6 mM TMB, 0.6 mM H_2O_2, 10 μg mL^{-1} 4Fe–Ni–B, HAc–NaAc buffer solution (pH = 3.5, 0.2 M), and different concentrations of GSH were added to the EP tube in a total volume of 2.0 mL. The solution was incubated for 2.0 min at room temperature. The absorbance of the solution at 652 nm was recorded. The experiments were performed under the same conditions in triplicate. Yili milk was purchased from supermarkets. The milk was centrifuged for 45 minutes and filtered to obtain a supernatant, which was diluted 100 times. Standard GSH solutions (5.0, 10.0, and 15.0 μM) were then added to the actual samples.

3 Results and discussion

3.1 Characterization of nanoenzymes

In order to elucidate the structural attributes of the metal borides, we performed an XRD analysis, the findings of which are presented in Fig. S1.† The XRD patterns uniformly indicated that the synthesized samples exhibited a broad diffraction peak within the range of 40° to 50°. This consistent observation corroborates with existing literature, thereby affirming the amorphous characteristic of the nanoparticles.[28]

SEM and TEM were employed to scrutinize the morphology of 4Fe–Ni–B nanoparticles, as illustrated in Fig. 1A–D. The 4Fe–Ni–B nanoparticles presented a uniform granularity morphology with particle dimensions ranging from 30 to 50 nm. The TEM image of 4Fe–Ni–B in Fig. 1C and D confirms the granular structure
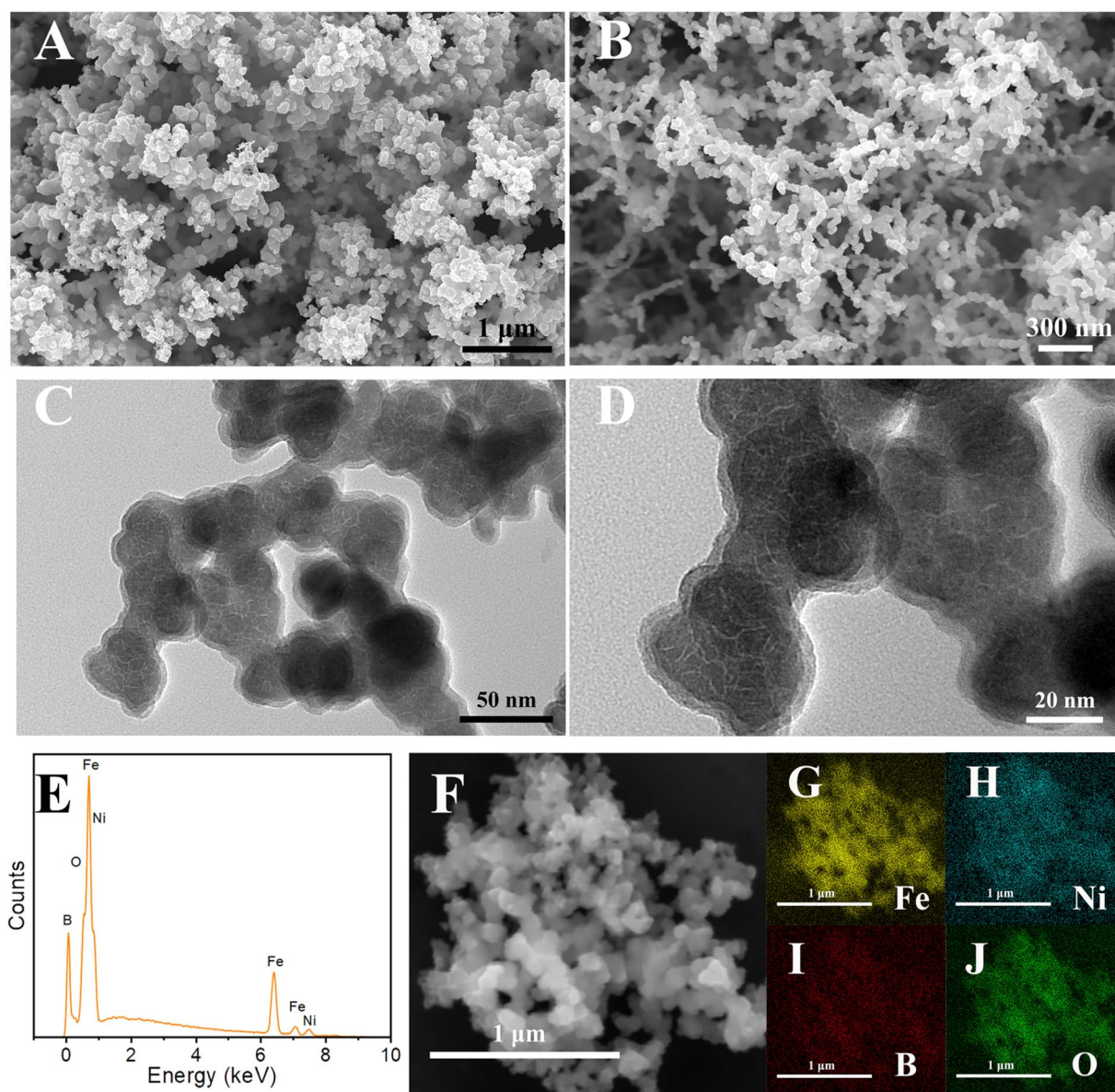

Fig. 1 (A and B) SEM images of 4Fe−Ni−B; (C and D) TEM images of 4Fe−Ni−B; (E) EDS spectrum of 4Fe−Ni−B; (F–J) element mapping images of Fe, Ni, B, O.

consisting of aggregated nanoparticles. ICP-OES analysis revealed that the Fe/Ni ratio in the 4Fe–Ni–B was found to be 4 : 1, closely matching the ratio of the starting materials, as depicted in Fig. S2.† The EDS spectra depicted in Fig. 1E unequivocally confirm the presence of Ni, Fe, B, and O elements within the product. The detection of elemental oxygen is ascribed to the partial oxidation of the nanoparticles.[36] Moreover, the uniform distribution of Fe, Ni, B, and O atoms across the 4Fe–Ni–B structure, as evidenced in Fig. 1 panels F, G, H, I, and J, corroborates the successful synthesis of the metal borides.

The specific surface areas of the catalysts, as ascertained by the BET method, are detailed in Table S1,† and these results suggest that the specific surface areas are not the dominant factor affecting the catalyst activity. The BET surface area of 4Fe–Ni–B nanoparticles is about 35.77 m^2 g^{-1}. The N_2 adsorption–desorption isotherms, presented in Fig. S3,† display a distinctive H3 hysteresis loop, which is characteristic of a type IV curve. Additionally, the pore size distribution curve in Fig. S3† demonstrated the presence of mesopores within the samples.

X-ray photoelectron spectroscopy (XPS) analysis was performed to ascertain the surface elemental composition and the nature of chemical bonding within the samples. The XPS survey spectrum of the 4Fe–Ni–B, depicted in Fig. 2A, verified the presence of Fe, Ni, and B elements on the surface. In the Fe 2p

spectrum shown in Fig. 2B, the peaks located at 709.9 and 723.6 eV correspond to Fe $2p_{3/2}$ and Fe $2p_{1/2}$ of the Fe^{2+} state, respectively. The peaks observed at 711.5 and 725.9 eV are Fe $2p_{3/2}$ and Fe $2p_{1/2}$ for the Fe^{3+} state, respectively, and the peak located at 719.4 eV corresponds to a satellite peak. Additionally, a peak at 706.5 eV is observed, which corresponds to Fe $2p_{3/2}$ in the Fe^0 state.[3] In the Ni 2p spectrum illustrated in Fig. 2C, the peak at 852.3 eV is attributed to the Ni $2p_{3/2}$ of the Ni^0 state, whereas the peak at 855.7 eV corresponds to Ni $2p_{3/2}$ of the Ni^{2+} state. 873.3 eV corresponds to Ni $2p_{1/2}$ of the Ni^{3+} state, and the rest of the peaks belong to satellite peaks.[28] It is noteworthy that the peak intensity of Ni^{2+} is markedly higher than that of Ni^{3+}. In the B 1s spectrum shown in Fig. 2D, the peak at 187.5 eV corresponds to the binding energy of boron in the metal boride, and the peak at 191.5 eV corresponds to the binding energy of boron oxide.[37] Meanwhile, the XPS spectrum for Fe–B is displayed in Fig. 2A. Synthesized using the same method as 4Fe–Ni–B, Fe–B lacks the Ni element as observed in Fig. 2A, but exhibits similar peaks in the Fe 2p spectrum in Fig. 2B and B 1s spectrum in Fig. 2D regions. By analyzing the peak areas presented in Fig. 2B and C, the molar ratio of Fe^{2+} to Fe^{3+} was determined to be 0.77 for Fe–B and 1.42 for 4Fe–Ni–B, while the ratio of Ni^{2+} to Ni^{3+} in 4Fe–Ni–B was found to be 3.28. These findings suggest that the incorporation of Ni^{2+} leads to an elevation in the Fe^{2+} content.[3]
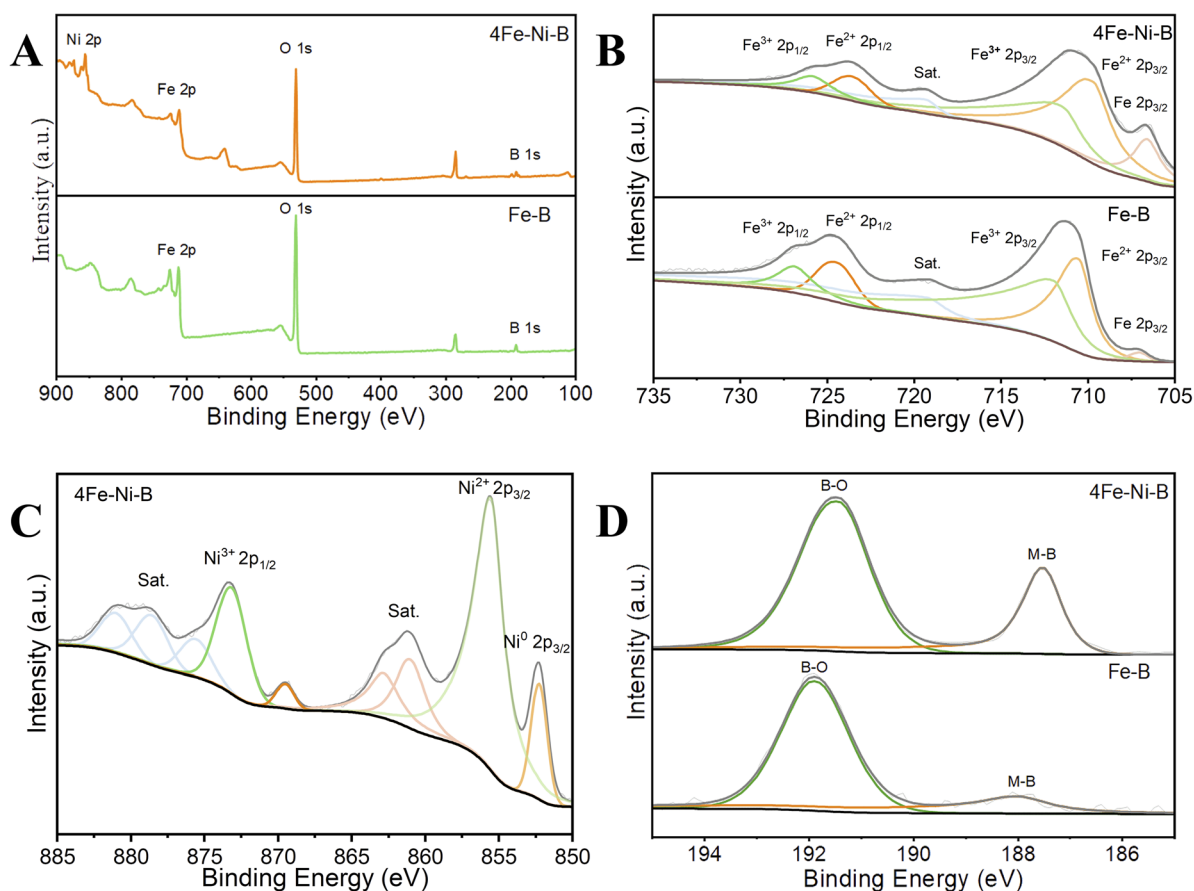

Fig. 2 XPS spectra of 4Fe–Ni–B and Fe–B (A); (B) Fe 2p; (C) Ni 2p; (D) B 1s.

3.2 Peroxidase-like activity

The peroxidase-like activity of nanozymes was assessed using H_2O_2 and TMB as substrates, with the results depicted in Fig. 3A. A distinct color change from colorless to blue was observed within a short timeframe of 2.0 minutes, indicative of robust catalytic activity. The absorbance at 652 nm served as a quantitative measure for characterizing the peroxidase-like activity of the nanozymes, as per established spectrophotometric methods.[38,39] It was demonstrated that when TMB and H_2O_2 were added to solutions containing Fe–B, 2Fe–3Ni–B, 3Fe–2Ni–B, 4Fe–Ni–B, and 4.5Fe–0.5Ni–B, respectively, oxTMB was formed, and the solutions changed from colorless to blue. This indicates that these samples have peroxidase-like activity. The order of activity from high to low is 4Fe–Ni–B, 4.5Fe–0.5Ni–B, Fe–B, 3Fe–2Ni–B, and 2Fe–3Ni–B. However, the formation of an oxTMB was not observed upon adding TMB and H_2O_2 to the solution containing Ni–B. This result indicates that Ni–B does not exhibit peroxidase-like activity.

The nanozyme candidate selected for further analysis was 4Fe–Ni–B, as illustrated in Fig. 3B. Notably, the solutions containing 4Fe–Ni–B + H_2O_2 and TMB + H_2O_2 showed no discernible change in color. The solution of 4Fe–Ni–B + TMB displayed a weak blue (oxTMB) color change, while the solution of 4Fe–Ni–B + H_2O_2 + TMB displayed a color variation from clear to blue, with a distinct absorption peak at 652 nm. The results indicate that 4Fe–Ni–B has an intrinsic peroxidase-like activity and could potentially possess oxidase-like activity.

3.3 Optimization of reaction conditions

To ascertain the optimal conditions for the peroxidase-like activity of 4Fe–Ni–B, a comprehensive evaluation of its catalytic activity was performed across a range of variables. This systematic investigation encompassed a spectrum of pH levels from 2.0 to 6.0, temperatures ranging from 25 to 45 °C, 4Fe–Ni–B nanozyme concentration from 2.5 to 20 μg mL^{-1}, reaction time from 30 to 300 s, TMB concentration varying between 0.2 to 1.4 mM, and H_2O_2 concentration spanning from 0.2 to 1.6 mM. The results, as illustrated in Fig. S4A† to F, revealed that the

catalytic activity of 4Fe–Ni–B was optimized at a pH of 3.5, a temperature of 25 °C, and a nanoenzyme concentration of 10 μg mL^{-1}, with both TMB and H_2O_2 substrate concentrations optimized at 0.6 mM. The reaction time was set to 120 s to facilitate subsequent testing.

3.4 Steady-state dynamics

Under the conditions of pH 3.5 and a temperature of 25 °C, a solution containing 4Fe–Ni–B at a concentration of 10 μg mL^{-1} along with H_2O_2 was introduced to an acetate buffer solution with TMB, and the mixture was incubated for 2.0 minutes to reach a steady state. The steady-state kinetic parameters for the nanoenzyme-catalyzed reactions with TMB and H_2O_2 as substrates were determined using the methodologies outlined in eqn (S1) and (S2),† with the results presented in Fig. S5.† The Michaelis–Menten kinetics, depicted in Fig. S5A and C,† illustrate the typical hyperbolic curves that characterize enzyme kinetics. The corresponding Lineweaver–Burk double reciprocal plots, shown in Fig. S5B and D† demonstrate a good linear relationship, indicative of a valid kinetic analysis. The K_m and V_{max} values for 4Fe–Ni–B are detailed in Table 1, alongside comparative data from referenced studies. The K_m value serves as a measure of the enzyme's affinity for its substrate—lower K_m values signifying higher affinity. Meanwhile, a higher V_{max} value is indicative of greater enzymatic activity.[45] The K_m for 4Fe–Ni–B with H_2O_2 as the substrate was determined to be nearly 20 times lower than that of horseradish peroxidase (HRP), signifying a markedly higher affinity of 4Fe–Ni–B for H_2O_2 compared to both HRP and other referenced peroxidase-like active nanomaterials. Moreover, when TMB was utilized as the substrate, the K_m value for 4Fe–Ni–B was measured at 0.394 mM, which is marginally lower than the reported value for natural HRP at 0.434 mM. Additionally, the V_{max} values obtained for 4Fe–Ni–B surpassed those recorded for HRP and the nanoenzymes documented in the literature. Collectively, these findings underscore the superior catalytic activity of 4Fe–Ni–B in its interactions with TMB. It is also noteworthy that our experiments were conducted at a lower temperature of 25 °C, which is
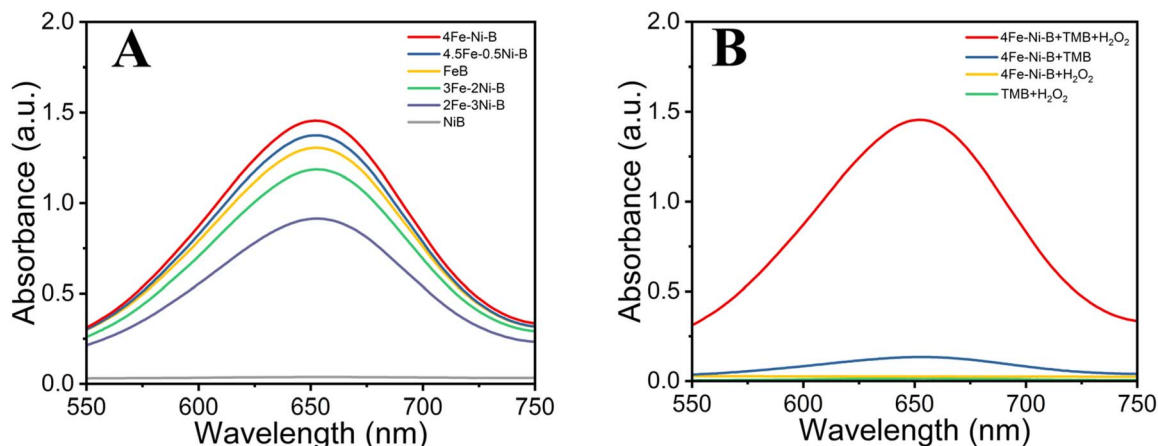

Fig. 3 UV-Vis absorption spectra of the oxidized TMB in different systems: (A) different nanozymes; (B) 4Fe–Ni–B + TMB + H_2O_2; 4Fe–Ni–B + TMB; 4Fe–Ni–B + H_2O_2; and TMB + H_2O_2.

Table 1 Kinetic parameters of different nanozymes

Sample	K_m (mM)		V_m (10^{-6} M s^{-1})		°C	Ref.
	TMB	H$_2$O$_2$	TMB	H$_2$O$_2$		
Fe$_{0.6}$Ni$_{0.4}$S	0.797	0.123	0.172	0.172	25	3
Fe$_{0.4}$Ni$_{0.6}$S	0.916	0.252	0.102	0.145	25	3
FeSe	0.009	8.09	0.042	0.065	25	40
FeS$_2$ NPs	0.17	0.30	0.039	0.056	45	21
FeS$_2$@C NS	0.16	0.46	0.062	0.119	45	41
NiS	0.241	0.347	0.051	0.053	25	42
CuZnFeS	2.2	0.07	0.39	0.005	37	43
CuS	0.007	12.0	0.089	0.209	40	44
HRP	0.434	3.70	0.1	0.087	35	6
Fe$_4$Ni$_1$B	0.394	0.183	0.513	0.433	25	This work

more convenient than the elevated temperatures of 35, 37, 40, and 45 °C referenced in the literature.

3.5 Mechanism of action of nanoenzymes

To elucidate the catalytic mechanism of the nanozyme, we carried out free radical trapping experiments on the system using EPR, as illustrated in Fig. 4A–C. 5-Dimethyl-1-pyrroline-*N*-oxide (DMPO) was selected as a spin trapper for the detection of ˙OH radical and ˙O$_2^-$ radical, while 2,2,6,6-tetramethylpiperidine (TEMP) was employed to detect ^{1}O$_2$.[46] The results demonstrated that 4Fe–Ni–B was competent in generating the distinctive absorption peaks corresponding to these three radicals as illustrated in Fig. 4A–C. Specifically, Fig. 4A exhibited a peak intensity ratio of 1 : 2 : 2 : 1, which is indicative of DMPO-˙OH adducts. The Fe^{2+} and Fe^{3+} ions within the 4Fe–Ni–B structure serve as the active sites for the formation of ˙OH radicals, as shown in eqn (5) and (6).[31] In addition, thiourea, *p*-benzoquinone, and tryptophan were added to the initial solution as traps for ˙OH, ˙O$_2^-$ and ^{1}O$_2$, respectively.[47–49] Fig. S6† illustrates the significant decrease in absorbance at 652 nm for solutions containing thiourea and *p*-benzoquinone upon the introduction of trapping agents. This decrease suggests the formation of ˙OH and ˙O$_2^-$ radicals during the reaction. Conversely, an increase in absorbance at 652 nm was observed for the solution containing tryptophan, which does not confirm the absence of ^{1}O$_2$ formation. The detection of free radicals using radical trappers is a common approach to determine if homogeneous catalysis involves free radicals. However, in the
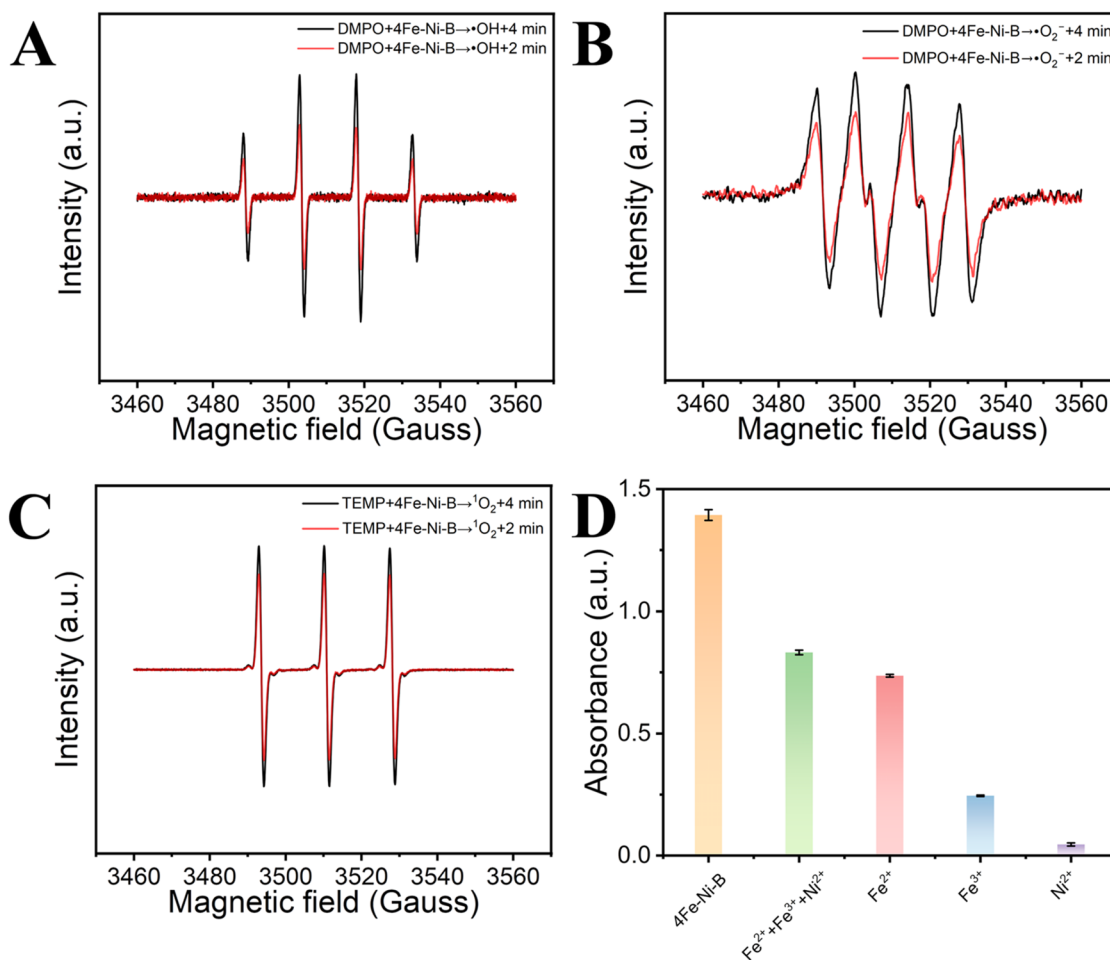

Fig. 4 EPR spectra of DMPO spin trapping in the solution of ˙OH and ˙O$_2^-$ (A) and (B); EPR spectrum of TEMP spin trapping in the solution of ^{1}O$_2$ (C); comparison of peroxidase activities of 4Fe–Ni–B, Fe^{2+} + Fe^{3+} + Ni^{2+}, Fe^{2+}, Fe^{3+} and Ni^{2+}, and ion concentrations were the same as those in the ICP experiment (D).

context of nano-enzymatic catalysis, this method cannot discern whether the trapped species are free radicals or reaction intermediates that are adsorbed onto the nanoscale surface.[39]

In order to determine the contribution of non-metallic boron to the peroxidase-like activity of 4Fe–Ni–B, we conducted a controlled experiment where the nanozyme was substituted with a mixture of Fe^{2+}, Fe^{3+}, and Ni^{2+} under identical optimal conditions. The catalytic activities of these ions were assessed, and their absorbance values at 652 nm were compared to those of 4Fe–Ni–B, as depicted in Fig. 4D. The comparative analysis revealed a descending order of catalytic activity: 4Fe–Ni–B exhibited the highest activity, followed by the mixture containing Fe^{2+}, Fe^{3+}, and Ni^{2+}, with Fe^{2+} showing notable activity and negligible activity observed for Ni^{2+}. These findings underscore the significant role of non-metallic boron in enhancing the peroxidase-like activity of 4Fe–Ni–B nanoenzymes, highlighting its indispensable function in the catalytic process.[3,31]

To gain insights into the catalytic reaction mechanisms, we employed density functional theory (DFT) calculations to delineate the potential pathways and the associated free-energy landscapes for the generation of $\cdot OH$, $\cdot O_2^-$, and $^1O_2$ from H_2O_2 for both 4Fe–Ni–B and Fe–B models, as depicted in Fig. 5A–C,

and S7.† The introduction of the Ni catalytic cofactor near the catalytic active site of Fe–B effectively reduced the energy of the Fe–B catalysts compared to Fe–B without the introduction of the Ni catalytic cofactor. The whole catalytic process generates three radicals from two pathways. In the homolytic pathway, the activated $*H_2O_2$ dissociates uniformly into two $*OH$ on the Fe site and Ni site and gradually desorbs from the surface to constitute $\cdot OH$ (eqn (1)).[50] In the heterolytic pathway, the revitalised $*H_2O_2$ dissociates and heterogeneously converts into $*OH$ and H_2O, and the formation of $*OH$ could react with H_2O_2 to form $*OOH$ (eqn (2)), which is degraded further to $\cdot O_2^-$ (eqn (3)).[51] Furthermore, $*OOH$ can also be converted to $^1O_2$ through the path of eqn (4).[52] As shown in Fig. 5B and C, the free energy changes of radicals produced by 4Fe–Ni–B are −1.47 eV, −1.67 eV, −1.42 eV, −1.78 eV, and −1.47 eV; these values are lower than those on the corresponding Fe–B models, which are −0.71 eV, −1.43 eV, −1.57 eV, −1.46 eV, −0.71 eV, −1.82 eV, −1.65 eV, and −2.02 eV, respectively. This disparity suggests that 4Fe–Ni–B more readily adsorbs H_2O_2 and reaction intermediates compared to the Fe–B models.[53] Additionally, an analysis of the charge density differences between the 4Fe–Ni–B and Fe–B models presented in Fig. S8A and B† reveals that the
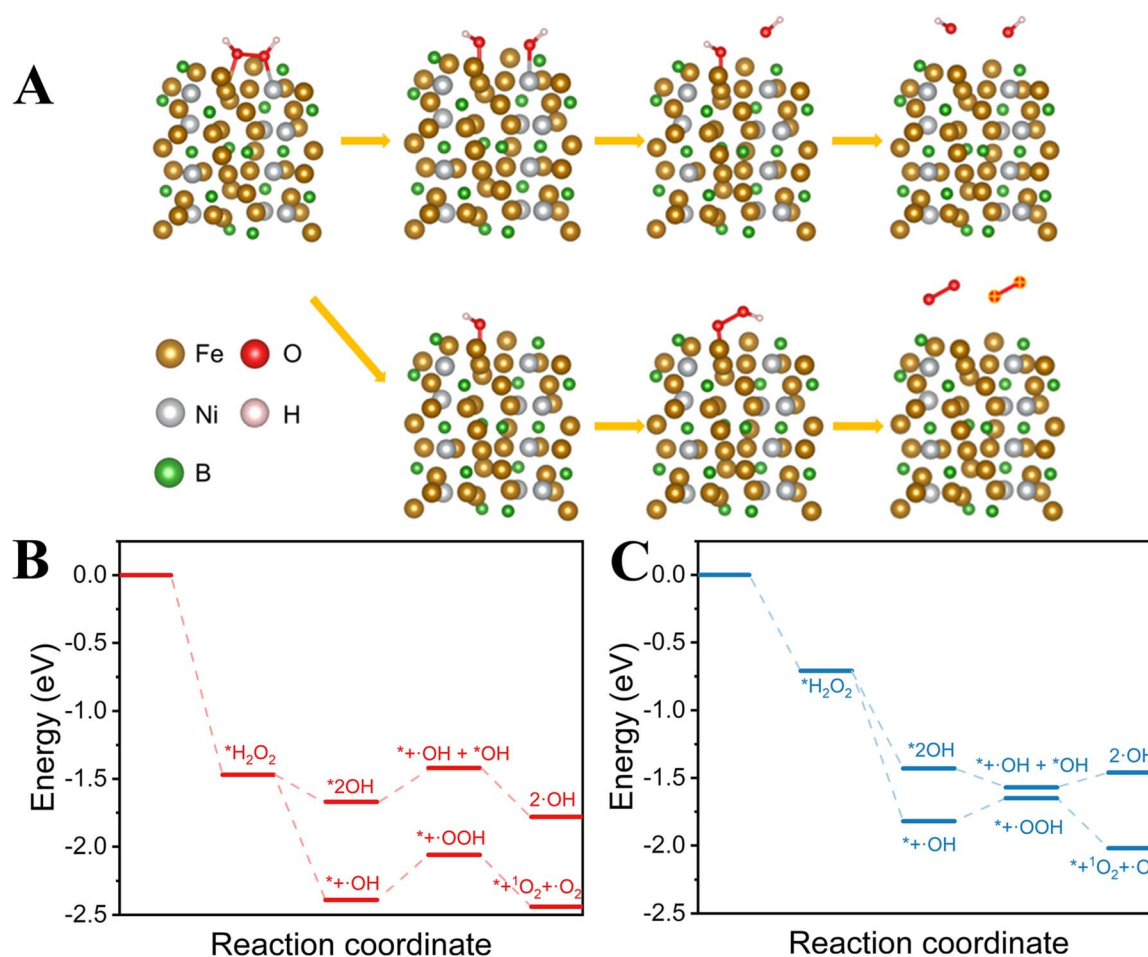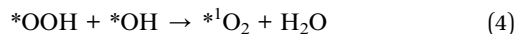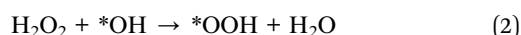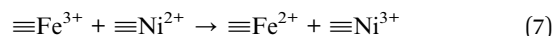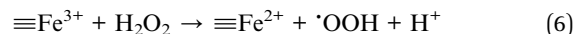

Fig. 5 The POD-like mechanism of 4Fe–Ni–B was investigated by DFT calculations. (A) POD-like catalytic mechanism of 4Fe–Ni–B (B) Gibbs free energy diagram of the POD-like mechanism on 4Fe–Ni–B (C) Gibbs free energy diagram of the POD-like mechanism on Fe–B.

incorporation of the Ni catalytic cofactor leads to a significant increase in electron enrichment at the catalytic active site of the 4Fe–Ni–B model. Moreover, the presence of Ni metal has been shown to expedite electron transfer. As supported by existing literature,[54–56] an enrichment of electrons at the catalytically active center facilitates the decomposition of H_2O_2, indicating that 4Fe–Ni–B is more effective in catalyzing the decomposition of H_2O_2 than the Fe–B models and possesses enhanced electron transfer capabilities.

$$H_2O_2 \rightarrow \cdot OH + \cdot OH \tag{1}$$

$$H_2O_2 + {}^*OH \rightarrow {}^*OOH + H_2O \tag{2}$$

$${}^*OOH \rightarrow H^+ + \cdot O_2^- \tag{3}$$

$${}^*OOH + {}^*OH \rightarrow {}^{*1}O_2 + H_2O \tag{4}$$

Drawing from our experimental findings, we have formulated a peroxidase (POD)-like mechanism for the 4Fe–Ni–B nanozyme. Initially, it was observed from the peroxidase-like activity assays, as presented in Fig. 3A, that the Ni–B counterpart displayed an absence of POD-like activity. We hypothesize that the incorporation of an optimal quantity of nickel ions into Fe–B substantially amplifies its enzymatic catalytic activity. This augmentation is potentially attributable to the formation of a bridge within the 4Fe–Ni–B structure, where the bonds between Fe and B and between Ni and B facilitate an internal electron transfer from $\equiv Ni^{2+}$ to $\equiv Fe^{3+}$. This transfer accelerates the Fe^{3+}/Fe^{2+} redox cycle, as illustrated in eqn (7), a pivotal process in the generation of radical production during enzyme-mimetic catalysis.[31] The presence of $\equiv Ni^{3+}$ in 4Fe–Ni–B, confirmed by XPS analysis, further substantiates the occurrence of electron transfer, a phenomenon also observed in other systems such as FeNi-MOF, FeNi sulfides, and CuFeNi hydroxides.[31–33] Conversely, an excess of Ni^{2+} in the metal borides leads to the occupation of active sites $\equiv Fe^{2+}$ and $\equiv Fe^{3+}$ by Ni ions, resulting in diminished catalytic activity. Taking these factors into account, the observed hierarchy of enzyme-like activity (4Fe–Ni–B > 4.5Fe–0.5Ni–B > Fe–B > 3Fe–2Ni–B > 2Fe–3Ni–B > Ni–B) is deemed logical and justifiable. The proposed peroxidase mechanism for 4Fe–Ni–B is depicted in Fig. S9.†

$$\equiv Fe^{2+} + H_2O_2 + H^+ \rightarrow \equiv Fe^{3+} + \cdot OH + H_2O \tag{5}$$

$$\equiv Fe^{3+} + H_2O_2 \rightarrow \equiv Fe^{2+} + \cdot OOH + H^+ \tag{6}$$

$$\equiv Fe^{3+} + \equiv Ni^{2+} \rightarrow \equiv Fe^{2+} + \equiv Ni^{3+} \tag{7}$$

3.6 Detection of H_2O_2

We have developed a simple and efficient colorimetric method for the quantification of H_2O_2, leveraging the inherent peroxidase-like activity of 4Fe–Ni–B. In this assay, TMB was employed as a chromogenic substrate, which, upon oxidation, transforms into a blue-colored oxidation product, oxTMB.[57] As shown in Fig. 6A, the absorbance measurements at 652 nm were conducted over a wide H_2O_2 concentration range, from 2.5 to 200 μM, under the most favorable reaction conditions. There was a good linear relationship between the increasing concentrations of H_2O_2 and the corresponding absorbance values. Fig. 6B presents a remarkable linear correlation between the absorbance at 652 nm and the H_2O_2 concentration, specifically within the range of 10.0 to 100.0 μM ($R^2 = 0.998$), achieving an LOD of 2.84 μM. Comparative experimental data from the literature featuring nanozymes analogous to 4Fe–Ni–B are compiled in Table S2.† Collectively, these findings underscore the high sensitivity and rapid response characteristics of 4Fe–Ni–B for H_2O_2 detection.

In order to evaluate the feasibility of our method in practical scenarios, we analyzed the levels of H_2O_2 in milk samples. Optimal reaction conditions were employed, and specific concentrations of H_2O_2 standards (20.0, 40.0, and 80.0 μM) were added to the diluted milk samples. Subsequently, the absorbance at 652 nm was recorded. Recovery rates were determined
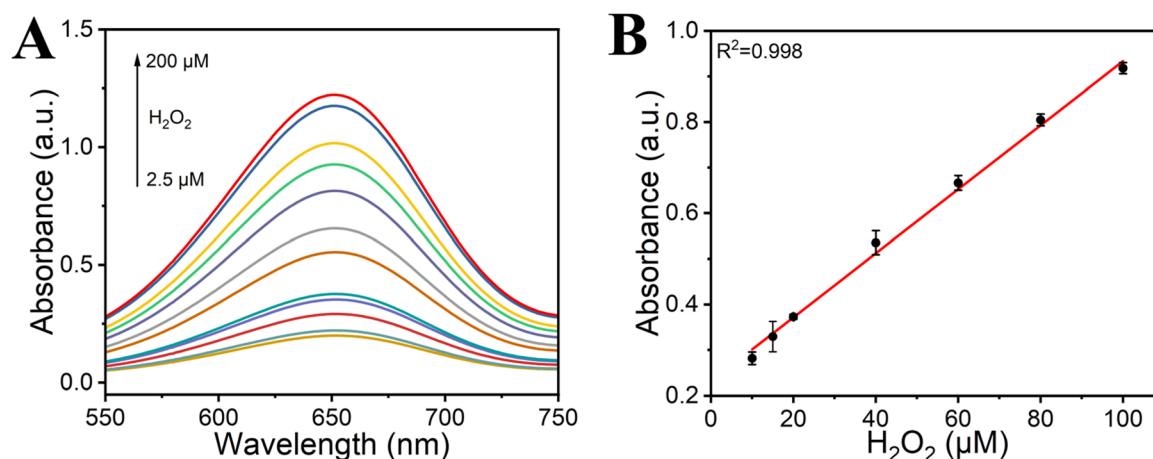

Fig. 6 Detection of H_2O_2 by 4Fe–Ni–B: (A) different of H_2O_2 concentrations; (B) the linear relationship between the absorbance of the solution at 652 nm and H_2O_2 concentration.

utilizing a linear standard curve, and the results are detailed in Table S3.† The recoveries fell within a range of 101.1% to 107.9%, and the relative standard deviations (RSD) of the whole samples were less than 1.70%. These results highlight the exceptional sensitivity of 4Fe–Ni–B and affirm its viability as an effective nanozyme for the detection of H_2O_2 in real-world samples.

3.7 Detection of glutathione

GSH is recognized for its inhibitory effects on peroxidase reactions, which can occur through several pathways, such as the reduction of peroxides, strong binding to nanozymes, scavenging of free radicals, and the reduction of oxTMB.[58,59] Our experimental data indicate that the reduction of oxTMB is the primary mechanism by which GSH suppresses the intrinsic peroxidase-like activity of 4Fe–Ni–B (eqn (8) and (9)). Building on this insight, we have developed a simple and rapid colorimetric assay for GSH detection, with TMB serving as the indicator. In the absence of GSH, colorless TMB is oxidized to blue oxTMB; however, the presence of GSH interferes with this oxidation process due to its reducing properties, thereby hindering the formation of blue oxTMB. Fig. 7A presents the results of the colorimetric assay for GSH, showing a measurable decrease in solution absorbance as GSH concentration increases from 0 to 320 µM under optimal conditions. Fig. 7B demonstrates a strong linear correlation between absorbance at

652 nm and GSH concentration within the range of 1.25 to 20 µM ($R^2 = 0.995$), with LOD of 2.97 µM. Comparative data from the literature featuring nanozymes analogous to 4Fe–Ni–B are compiled in Table S2,† confirming that 4Fe–Ni–B offers a sensitive and swift detection method for GSH.

Selectivity is an important measure of the anti-interference performance of a colourimetric sensor. In this experiment, a variety of common interfering substances were added to the mixed system, including amino acids, glucose, and ascorbic acid, amongst others. The results of this assessment are shown in Fig. 7C and D. The results show that in selectivity experiments, 4Fe–Ni–B shows a high level of selectivity for GSH detection despite the addition of 10-fold more interfering chemicals than GSH. In contrast, in the anti-interference experiments, only one class of strongly reducing substances, such as ascorbic acid and cysteine, interfered with the 4Fe–Ni–B sensor. This means that it has the potential to accurately quantify GSH even in the presence of other biomolecules.

In order to evaluate the feasibility of our method in practical scenarios, we analyzed the levels of GSH in milk samples. Optimal reaction conditions were employed, and specific concentrations of GSH standards (5.0, 10.0, and 15.0 µM) were added to the diluted milk samples. Subsequently, the absorbance at 652 nm was recorded. Recovery rates were determined utilizing a linear standard curve, and the results are detailed in Table S3.† The recoveries fell within a range of 103.3% to 104.8%, while the relative standard deviations were between
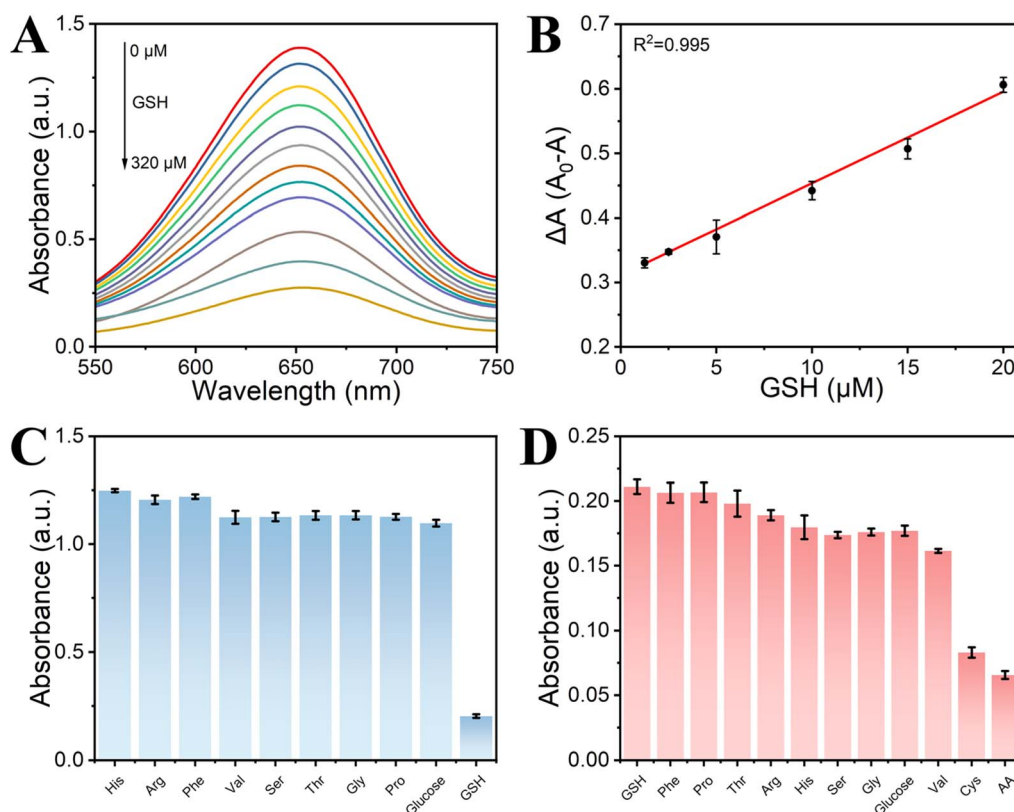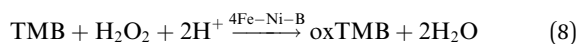

Fig. 7 Detection of GSH by 4Fe–Ni–B: (A) different of GSH concentrations; (B) the linear relationship between the absorbance of the solution at 652 nm and GSH concentration; (C) selectivity of the 4Fe–Ni–B for GSH; (D) immunity of the 4Fe–Ni–B for GSH.

0.9% and 1.7%. These results highlight the exceptional sensitivity of 4Fe–Ni–B and affirm its viability as an effective nanozyme for the detection of GSH in real-world samples.

In addition, the stability and recoverability of the nanozyme are important parameters for the evaluation of colorimetric sensors. Although 4Fe–Ni–B has been stored for about 12 months, its XRD profile remained consistent with the initially prepared XRD profile, as shown in Fig. S11A.† Meanwhile, we also investigated the catalytic activity of the 4Fe–Ni–B solution at 6 h. The catalytic activity of 4Fe–Ni–B at 6 h was the same as that of the initially prepared 4Fe–Ni–B catalytic activity, as shown in Fig. S11B.† Finally, our analysis of the 4Fe–Ni–B nanozyme was evaluated in the recoverability experiments, as shown in Fig. S12.† The 4Fe–Ni–B pre-reaction XRD and post-reaction XRD spectra remained essentially the same. The results show that 4Fe–Ni–B has good stability and recoverability.

$$TMB + H_2O_2 + 2H^+ \xrightarrow{4Fe-Ni-B} oxTMB + 2H_2O \quad (8)$$

$$oxTMB + 2GSH \xrightarrow{4Fe-Ni-B} TMB + GSSH + 2H^+ \quad (9)$$

4 Conclusions

In summary, we successfully synthesized amorphous metal boride nanoparticles *via* a straightforward chemical reduction approach conducted under chilled conditions. In a pioneering study, we explored the peroxidase-like activity of these metal boride nanoparticles and identified 4Fe–Ni–B as the standout candidate with the most robust peroxidase-like activity. The catalytic behavior of 4Fe–Ni–B was found to adhere to the well-established Michaelis–Menten kinetic model. This nanomaterial offers a suite of benefits, including its low cost, ease of synthesis, and exceptional reproducibility. The development of a colorimetric sensor for H_2O_2 and GSH detection, coupled with the revelation of the synergistic effect between Ni^{2+} and Fe^{3+} ions, highlights the significant potential of 4Fe–Ni–B as a cutting-edge artificial enzyme. Our research not only extends the utility of binary metal borides in analytical and diagnostic applications but also paves the way for the next generation of nanozymes designed with enhanced catalytic capabilities.

Data availability

Data will be available on request.

Author contributions

Si-Hua Deng and Yi-Fan Han carried out the chemical investigations; Si-Hua Deng and Qi Zhou performed experiments and data organization and prepared the draft manuscript. Ying-Zhao Ma and Wen-Sheng Fu supervised and validated the work.

Conflicts of interest

There are no conflicts to declare.

References

1 H. Jiang, Z. Chen, H. Cao and Y. Huang, *Analyst*, 2012, **137**, 5560–5564.
2 X. Wang, Y. Hu and H. Wei, *Inorg. Chem. Front.*, 2016, **3**, 41–60.
3 C. Zhang and Z. Nan, *J. Phys. Chem. C*, 2022, **126**, 4355–4364.
4 P. Ni, Y. Sun, H. Dai, J. Hu, S. Jiang, Y. Wang and Z. Li, *Biosens. Bioelectron.*, 2015, **63**, 47–52.
5 A. Afsah-Sahebi, S. S. Shahangian, H. Khodajou-Masouleh and R. H. Sajedi, *Spectrochim. Acta, Part A*, 2023, **290**, 122260.
6 L. Gao, J. Zhuang, L. Nie, J. Zhang, Y. Zhang, N. Gu, T. Wang, J. Feng, D. Yang, S. Perrett and X. Yan, *Nat. Nanotechnol.*, 2007, **2**, 577–583.
7 L. Han, H. Zhang, D. Chen and F. Li, *Adv. Funct. Mater.*, 2018, **28**, 1800018.
8 A. L. Hu, H. H. Deng, X. Q. Zheng, Y. Y. Wu, X. L. Lin, A. L. Liu, X. H. Xia, H. P. Peng, W. Chen and G. L. Hong, *Biosens. Bioelectron.*, 2017, **97**, 21–25.
9 X. Xu, Y. Shen, R. Xing, J. Kong, R. Su, R. Huang and W. Qi, *ACS Appl. Mater. Interfaces*, 2024, **16**, 21975–21986.
10 S. Li, H. Ding, J. Chang, S. Dong, B. Shao, Y. Dong, S. Gai, F. He and P. Yang, *J. Colloid Interface Sci.*, 2022, **623**, 787–798.
11 P. Li, Y. Li, M. Qi and X. Zhang, *Chem. Eng. J.*, 2024, **493**, 152686.
12 J. Wang, J. Liu, C. Zhou, Y. Lv, N. Wang, M. Li and X. Su, *Sens. Actuators, B*, 2024, **415**, 135954.
13 J. Yu, T. Chen, X. Wen, H. Shi, L. Wang and Y. Xu, *Biosens. Bioelectron.*, 2024, **253**, 116169.
14 F. Mao, Z. He, Z. Sun, S. Zhang, H. Cao and X. Liu, *Food Chem.*, 2024, **453**, 139623.
15 S. Yang, C. Li, Y. Yu, H. Zhan, J. Zhai, R. Liu, W. Chen, Y. Zou and K. Xu, *Sens. Actuators, B*, 2024, **404**, 135216.
16 L. Fan, L. Kong, H. Liu, J. Zhang, M. Hu, L. Fan, H. Zhu and S. Yan, *Biosens. Bioelectron.*, 2024, **250**, 116033.
17 C. Cheng, M. Han, G. Xiang, X. Fu, X. Wang and C. Lu, *Food Chem.*, 2024, **444**, 138667.
18 Z. Han, Q. Fu, Y. lv, N. Wang and X. Su, *Talanta*, 2024, **272**, 125704.
19 S. Chen, Y. Liu, Z. Qin, G. Wen and Z. Jiang, *Analyst*, 2024, **149**, 1179–1189.
20 X. Zhao, Z. Liu, Y. Qiu, Q. Zhang, Y. Chen, D. Wang, Z. Zhu, L. Meng and H. Zheng, *Anal. Chem.*, 2024, **96**, 12120–12128.

21 C. Song, W. Ding, W. Zhao, H. Liu, J. Wang, Y. Yao and C. Yao, *Biosens. Bioelectron.*, 2020, **151**, 111983.

22 H. Yang, J. Zha, P. Zhang, Y. Xiong, L. Su and F. Ye, *RSC Adv.*, 2016, **6**, 66963–66970.

23 B. He, L. Wang, X. Jin, X. Zhang, R. Sha, Y. Liang, Y. Wang, W. Xie, J. Shi and H. Peng, *Anal. Chem.*, 2024, **96**, 9167–9176.

24 E. Schneider, M. D. Tita, J. L. Guerreiro, A. J. Duarte and F. T. C. Moreira, *Anal. Methods*, 2024, **16**, 3663–3674.

25 C. Zhou, N. Wang, Y. Su, J. Liu, Y. Lv and X. Su, *Sens. Actuators, B*, 2024, **418**, 136246.

26 J. Wu, X. Wang, Q. Wang, Z. Lou, S. Li, Y. Zhu, L. Qin and H. Wei, *Chem. Soc. Rev.*, 2019, **48**, 1004–1076.

27 G.-Y. Chen, T.-Q. Chai, H. Zhang and F.-Q. Yang, *Coord. Chem. Rev.*, 2024, **508**, 215761.

28 G. Liu, D. He, R. Yao, Y. Zhao and J. Li, *Nano Res.*, 2018, **11**, 1664–1675.

29 C. Zhang and Z. Nan, *Inorg. Chem.*, 2022, **61**, 13933–13943.

30 H. Cheng, Y. Chen, M. Liu, H. Tao, L. Chen, F. Wang, L. Huang, J. Tang, T. Yang and R. Hu, *Chem. Sci.*, 2024, **15**, 14816–1482831.

31 H. Tan, C. Li and Z. Nan, *Dalton Trans.*, 2023, **52**, 12819–12831.

32 D. Wang, M. Suo, S. Lai, L. Deng, J. Liu, J. Yang, S. Chen, M.-F. Wu and J.-P. Zou, *Appl. Catal., B*, 2023, **321**, 122054.

33 Y. Xu, Y. Ma, X. Chen, K. Wu, K. Wang, Y. Shen, S. Liu, X. J. Gao and Y. Zhang, *Angew. Chem., Int. Ed.*, 2024, **63**, e202408935.

34 S. Wang, J. Zhao, L. Zhang, C. Zhang, Z. Qiu, S. Zhao, Y. Huang and H. Liang, *Adv. Healthcare Mater.*, 2022, **11**, 2102073.

35 X. Wang, M. Cao, X. Zhu, J. Yu, Y. Liu, A. Li and Y. Xu, *Chin. J. Chem.*, 2024, **42**, 2187–2196.

36 L. Hu, D. Zhao, C. Liu, Y. Liang, D. Zheng, S. Sun, Q. Li, Q. Liu, Y. Luo, Y. Liao, L. Xie and X. Sun, *Inorg. Chem. Front.*, 2022, **9**, 6075–6079.

37 J. M. V. Nsanzimana, Y. Peng, Y. Y. Xu, L. Thia, C. Wang, B. Y. Xia and X. Wang, *Adv. Energy Mater.*, 2018, **8**, 1701475.

38 F. Xia, Q. Shi and Z. Nan, *Dalton Trans.*, 2020, **49**, 12780–12792.

39 F. Xia, Q. Shi and Z. Nan, *Surf. Interfaces*, 2021, **24**, 101109.

40 A. K. Dutta, S. K. Maji, D. N. Srivastava, A. Mondal, P. Biswas, P. Paul and B. Adhikary, *ACS Appl. Mater. Interfaces*, 2012, **4**, 1919–1927.

41 W. Ding, H. Liu, W. Zhao, J. Wang, L. Zhang, Y. Yao, C. Yao and C. Song, *ACS Appl. Bio Mater.*, 2020, **3**, 5905–5912.

42 H. Liu, H. Ma, H. Xu, J. Wen, Z. Huang, Y. Qiu, K. Fan, D. Li and C. Gu, *Anal. Bioanal. Chem.*, 2019, **411**, 129–137.

43 A. Dalui, B. Pradhan, U. Thupakula, A. H. Khan, G. S. Kumar, T. Ghosh, B. Satpati and S. Acharya, *Nanoscale*, 2015, **7**, 9062–9074.

44 A. K. Dutta, S. Das, S. Samanta, P. K. Samanta, B. Adhikary and P. Biswas, *Talanta*, 2013, **107**, 361–367.

45 H. Sun, A. Zhao, N. Gao, K. Li, J. Ren and X. Qu, *Angew Chem. Int. Ed. Engl.*, 2015, **54**, 7176–7180.

46 Z. Lin, L. Zheng, W. Yao, S. Liu, Y. Bu, Q. Zeng, X. Zhang, H. Deng, X. Lin and W. Chen, *J. Mater. Chem. B*, 2020, **8**, 8599–8606.

47 W.-f. Wang, M. N. Schuchmann, H.-P. Schuchmann, W. Knolle, J. von Sonntag and C. von Sonntag, *J. Am. Chem. Soc.*, 1999, **121**, 238–245.

48 D. Sang, X. Li, Z. Xu, H. Lin, C. Guo and F. Qu, *Biomater. Sci.*, 2020, **8**, 6045–6055.

49 M. Wang, X. Zhou, S. Wang, X. Xie, Y. Wang and X. Su, *Anal. Chem.*, 2021, **93**, 3130–3137.

50 R. Sheng, Y. Liu, T. Cai, R. Wang, G. Yang, T. Wen, F. Ning and H. Peng, *Chem. Eng. J.*, 2024, **485**, 149913.

51 X. Bi, Q. Bai, L. Wang, F. Du, M. Liu, W. W. Yu, S. Li, J. Li, Z. Zhu, N. Sui and J. Zhang, *Nano Res.*, 2022, **15**, 1446–1454.

52 J. Wang, Z. W. Jiang and Y. Wang, *Sens. Actuators, B*, 2024, **415**, 136012.

53 S. Wei, W. Ma, M. Sun, P. Xiang, Z. Tian, L. Mao, L. Gao and Y. Li, *Nat. Commun.*, 2024, **15**, 6888.

54 Y. Dang, G. Wang, G. Su, Z. Lu, Y. Wang, T. Liu, X. Pu, X. Wang, C. Wu, C. Song, Q. Zhao, H. Rao and M. Sun, *ACS Nano*, 2022, **16**, 4536–4550.

55 Y. Feng, Y. Guan, E. Zhou, X. Zhang and Y. Wang, *Adv. Sci.*, 2022, **9**, 2201339.

56 X. Huang, F. Xia and Z. Nan, *ACS Appl. Mater. Interfaces*, 2020, **12**, 46539–46548.

57 E. Niki, *Br. J. Cancer, Suppl.*, 1987, **8**, 153–157.

58 E. A. Bump and J. M. Brown, *Pharmacol. Ther.*, 1990, **47**, 117–136.

59 G. Kresse and J. Furthmüller, *Comput. Mater. Sci.*, 1996, **6**, 15–50.